# Facility Development and Status



### **Status of TLS and TPS Accelerators**

#### Taiwan Light Source (TLS)

#### **Machine Parameters of the TLS**

The Taiwan Light Source (TLS) celebrated its 30<sup>th</sup> anniversary of its first operation in 2023. Since its commissioning in 1993, TLS has invited experimental proposals and opened its facilities to users, initially featuring three soft X-ray beamlines: HSGM, LSGM, and Seya. The original TLS design was based on a triple bend achromatic lattice with a beam energy of 1.3 GeV and a beam current of 200 mA. Following several phases of upgrades, the accelerator has now achieved a beam energy of 1.5 GeV, a maximum stored beam current of

Table 1: Main parameters of the TLS storage ring.

Beam Energy (GeV)	1.5
Number of Buckets	200
Current (mA)	360
Horizontal Emittance (nm-rad.)	22
Vertical Emittance (pm-rad.)	88
Tunes $(v_x/v_y)$	7.303/4.175
Lifetime (hour)	> 6

360 mA, top-up injection capabilities, a superconducting radio-frequency (SRF) cavity, a liquid-helium cryogenic system, superconducting wigglers (SCWs), and advanced feedback systems for orbit and bunch-to-bunch stability. Many of these advancements were pioneering and unique in the low-energy synchrotron community. The key parameters of TLS are presented in **Table 1**.

The storage ring, which is designed with sixfold symmetry, features four room-temperature undulators, one wiggler, and five SCWs, giving resulting in the most densely packed SCW configuration in the community for the TLS. SCWs enable the generation of high-energy photons to support X-ray users. The specifications of the insertion devices are listed in **Table 2**.

**Table 2**: Main parameters of the insertion devices used in the TLS.

	W200	U50	U90	EPU56	SWLS	SW60	IASWA	IASWB	IASWC
Type	Hybrid	Hybrid	Hybrid	Pure	SC	SC	SC	SC	SC
Period length (mm)	200	50	90	56	250	60	61	61	61
Photon energy (eV)	800–15k	60–1.5k	5-500	80-1.4k	2k-38k	5k-20k	5k-20k	5k-23k	5k-20k

#### **Statistics of TLS Machine Operation**

During the initial top-up injection phase, the stored beam current was limited to 200 mA in early 2005 because of the constraints of the radio frequency system capabilities and beam stability. Following the installation of the SRF module and the upgrade of the feedback system, TLS gradually increased the stored beam current to 360 mA after 2010. Figure 1 presents the performance metrics of TLS operations from 2011 to 2024. Availability is defined as the ratio of actual user time to scheduled user time; mean time between failures (MTBF) is defined as the ratio of scheduled user time to the number of system faults; and the beam stability index is evaluated based on photon intensity variation in the diagnostic beamline, maintained within 0.1%.



Fig. 1: Annual beam stability index of 0.1%, availability, and MTBF of the TLS.

In 2024, the annual availability of the TLS reached 99.4%, with scheduled user time totaling 4,578 hours, a second-highest MTBF of 286.1 hours, and a beam stability of 99.36%. After switching of the pulsed klystron supplier from Thales to Canon in 2023, the operational reliability and stability of the TLS linear accelerator system have significantly improved in 2024.

#### Downtime and Failure Analysis of the TLS

In 2024, there were 15 beam trips and a total of 28.35 hours of downtime. The SRF system, which provides high power to the stored beam and operates at 4.5 K, is complex and requires a strict interlock protection system. This system accounted for the largest portion of the annual downtime with a fast recovery time. The contributions from each subsystem of the TLS facility are shown in **Figs. 2 and 3**. The primary causes of downtime were force majeure and unknown events, including earthquakes and voltage drops at the power station. The second-most common cause of downtime was related to the instrumentation and control group (I&C), including issues such as FOFB, failures in the power supply of the 500 MHz master clock RF amplifier, and ILC failures. Alternative solutions for replacing failed and aging systems are currently being evaluated.

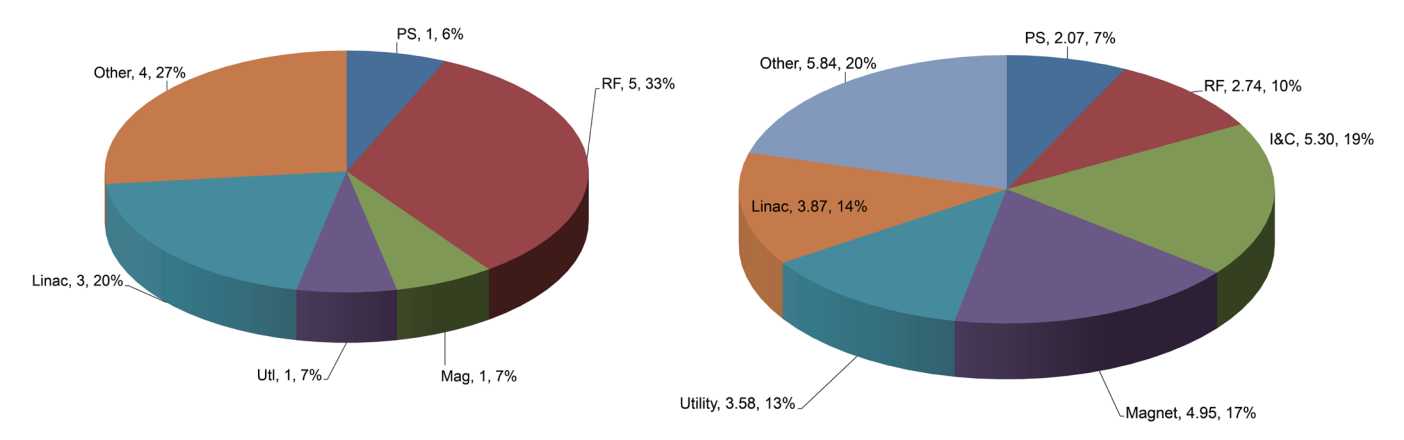


Fig. 2: Proportions of beam trips for the TLS accelerators in 2024 (15 trip events in total). RF stands for radio frequency; PS stands for power supply; and I&C stands for instrumentation & control. "Other" includes 1 earthquake, 1 voltage drop caused by Taiwan Power Company (TPC), and 2 unknown partial beam losses.

**Fig. 3:** Downtime distribution for the TLS accelerators in 2024 (totaling 28.35 hours). The major failure times were as follows: other, 5.84 hours; I&C, 5.3 hours; magnet, 4.95 hours; and Linac, 3.87 hours.

#### **Taiwan Photon Source (TPS)**

#### **Machine Parameters of the TPS**

The Taiwan Photon Source (TPS) has been operational for eight years, having officially been opened to users in 2016. The TPS storage ring incorporates a strong focusing double bend achromatic lattice, which features low emittance, top-up injection, SRF module operation, long straight sections, and high stability. The major parameters of the TPS storage ring for current operation are listed in **Table 3**. The TPS accelerators consist of concentric storage rings and booster rings within the same tunnel, a design choice made considering the limited space on the campus and energy conservation.

**Table 3**: Main parameters of the TPS storage ring.

Beam Energy (GeV)	3
Circumference (m)	518.4
Current (mA)	500
Number of Buckets	864
Beam Emittance $(\varepsilon_x/\varepsilon_y)$ (nm-rad.)	1.6/0.016
Momentum Compaction (α <sub>1</sub> /α <sub>2</sub> )	0.0024/0.0021
Tunes $(v_x/v_y)$	26.15/14.23
Lifetime (hour)	> 8

#### **Statistics of TPS Machine Operation**

The TPS began operations for users in the last quarter of 2016, with a beam current of 300 mA, which increased to 400 mA in December 2017. The system continued to operate regularly until it reached 450 mA on the last day of 2020. In 2021, the stored beam current reached an operating current of 500 mA. The COVID-19 pandemic caused delays in the delivery of several key components for the Phase-II and Phase-III beamlines. Despite these challenges, through dedicated collaboration between vendors and NSRRC staff, 18 beamlines were available for user operation in 2024.

**Figure 4** on the next page shows the scheduled and delivered user times and availability on a quarter-to-quarter basis since 2017. The scheduled user time in 2024 was 4,890 hours. Because of frequent earthquakes in Hualien from April to May, a total of 8 beam trips and a recovery time of 12.01 hours were recorded. As shown in **Fig. 5** on the next page, the annual availabilities with and without seismic induction statistics were 97.7% and 97.92%, and MTBF of 163 hours and 221.2 hours, respectively.

#### Downtime and Failure Analysis of the TPS

In 2024, there were 29 beam trips and a total downtime of 113.36 hours. With the 8 beam trips caused by earthquakes excluded, the contributions of each subsystem within the TPS facility to these beam trips and downtime are illustrated in Figs. 6 and 7. The subsystems most frequently involved in beam trips and downtime are the SRF and LINAC systems. The higher failure rate of the SRF system is attributed to sensor aging and solid-state module damage resulting from prolonged operation at a high current of 500 mA. For the LINAC system, the primary issue is the long recovery time caused by klystron failure. Nevertheless, excluding trips caused by earthquakes, the overall reliability of these subsystems has significantly improved in recent years, enabling stable operation and extending the MTBF. (Reported by Hung-Jen Tsai)

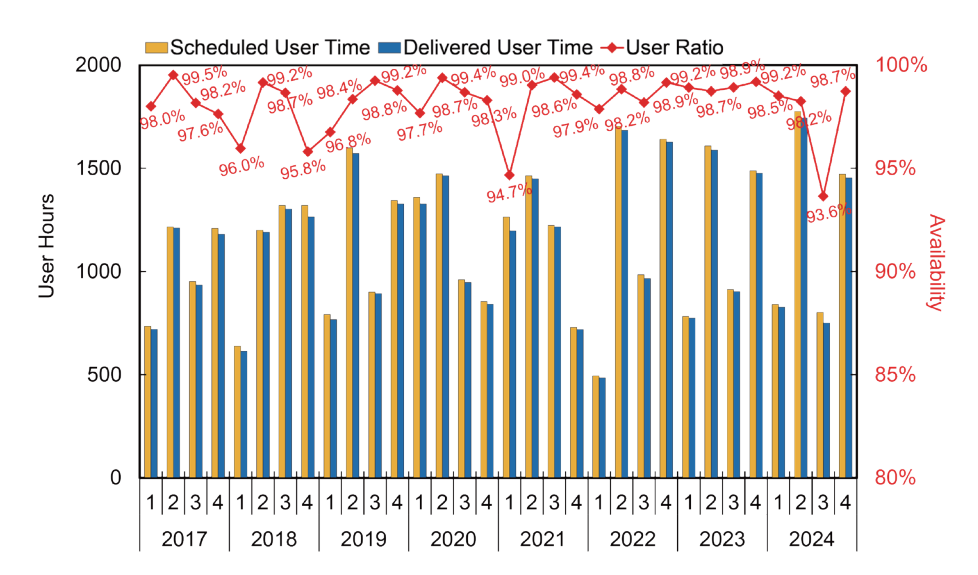


Fig. 4: User time and beam availability of the TPS from 2017 onward.

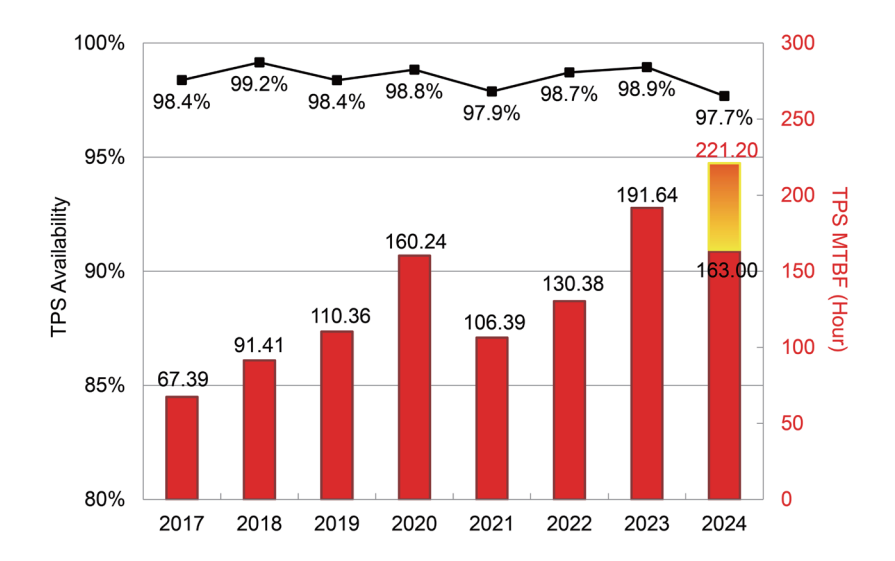
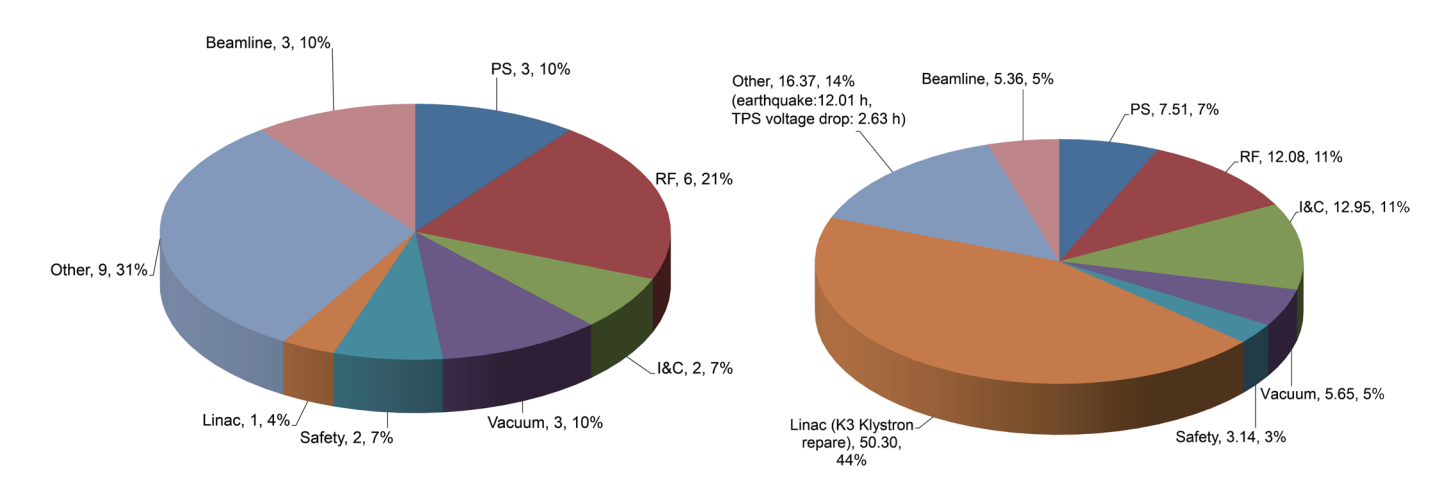


Fig. 5: MTBF and beam trip statistics of the TPS from 2017 onward. In 2024, the MTBF with and without seismic induction statistics was 163 hours and 221.2 hours, respectively.



**Fig. 6**: Proportions of beam trips of the TPS accelerators in 2024. There were 29 trip events in total. "Other" includes 8 earthquake events and 1 TPC voltage drop.

**Fig. 7:** Proportions of downtime in the TPS accelerators in 2024 (totaling 113.36 hours). The major failure times were as follows: Linac, 50.3 hours; other, 16.37 hours; I&C, 12.95 hours; and RF, 12.08 hours.

# **Elliptically Polarized Undulator Coupling Correction at the Taiwan Photon Source**

#### Introduction

Tive APPLE-II types of elliptically polarized undulators (EPUs) are installed in the Taiwan Photon Source (TPS) to produce elliptically polarized light, namely, EPU46-45, EPU48A-41, EPU48B-41, EPU168-39, and EPU66-27. An APPLE-II-type EPU comprises four identical quadrants of magnet arrays. By enabling the translation of two diagonal quadrants parallel to the magnetic axis while keeping the other two fixed, adjustments can be made to vary the strength of the horizontal and vertical magnetic field components  $(B_x \text{ and } B_y)$ , consequently influencing the ellipticity of the electron beam. Because of manufacturing imperfections in the EPU, it generates a skew quadrupole component that varies at different gaps and phases.

The residual skew quadrupole component couple horizontal betatron motion and dispersion to the vertical plane and then results in changes in beam size. When the electron beam encounters the residual skew quadrupole component of the EPU and subsequently traverses a region where vertical acceptance is minimal around the entire ring, there is a risk of beam scraping and loss.

To mitigate the coupling effects from the EPU and to maintain vertical beam size, each EPU is equipped with a pair of skew quadrupole magnets, named upstream skew quadrupole (USQ) and downstream skew quadrupole (DSQ), located at the entrance and exit of the EPU, respectively. This type of coupling correction is similar to the three-

magnet bump used for orbit correction.1 Since the residual skew quadrupole of the EPU varies with gaps and phases, a 2D coupling feedforward table that accounts for gap and phase for both USQ and DSQ is needed to compensate for the residual skew quadrupole from the EPU and to maintain the beam size. To build such a 2D coupling feed-forward table, an indicator beam loss monitor (BLM) is used to monitor the variations in the beam size. This method is fast and sensitive. If the beam size exceeds the vertical acceptance level, then the beam will be scraped and lost. Conversely, if the beam size remains smaller within the vertical acceptance, then the electron beam will not be scraped.

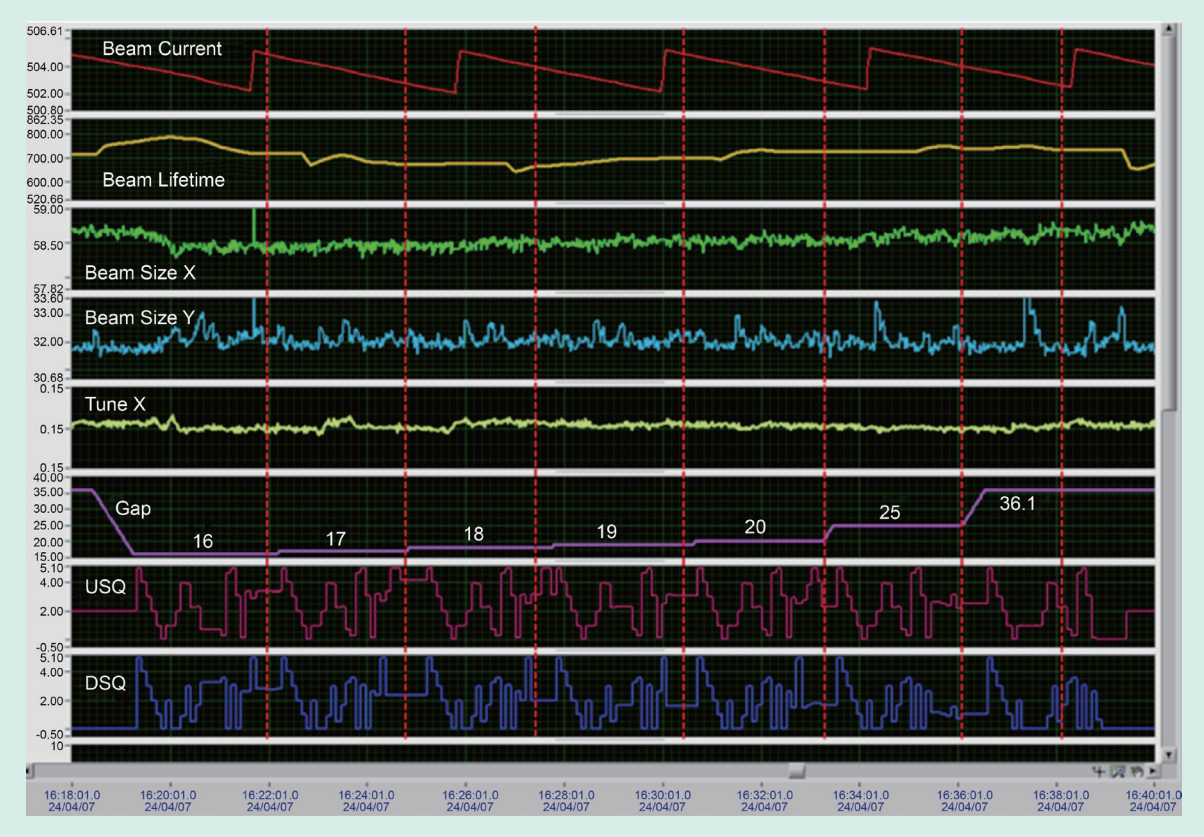


Fig. 1: Optimization process for EPU66-27 coupling feed-forward table by Bayesian optimization.

#### **Coupling Feed-Forward Table**

To counteract the undesired coupling effects caused by the residual skew quadrupole component of the EPU, it is essential to construct a 2D coupling feed-forward table based on the gap and phase of the EPU. For this purpose, an automatic measurement program that uses two nested loops to automatically adjust the gap and phase of the EPU has been developed. At each step of the gap and phase, the currents for the USQ and DSQ of the EPU are optimized to minimize the BLM reading using Bayesian optimization. The procedures for building the EPU coupling feedforward table are outlined as follows:

- 1. The gaps of all EPUs are ensured to be minimized to their lowest settings to provide appropriate vertical acceptance, while the TPS is operated in top-up injection mode with a beam current of 500 mA
- 2. Two nested loops are used to gradually adjust the gap and phase of the EPU to a specific setting and thus modify one gap or phase at a time.
- 3. For each gap and phase setting, the program automatically adjusts the currents of the USQ and DSQ of the EPU to minimize the BLM reading. The optimization should occur outside of injection periods.
- 4. Once the minimum BLM reading is achieved, the USQ and DSQ currents corresponding to that gap and phase setting are recorded by the program.
- 5. This process for each subsequent gap and phase is repeated, with the skew quadrupole currents adjusted and recorded at each step of gap and phase.

This procedure effectively builds the coupling feed-forward table, minimizing the coupling effects across all gap and phase settings of the EPUs. A shell script is then used to convert the 2D feed-forward table into a waveform format to enable the soft IOC to read it and perform interpolation. This allows the soft IOC to adjust the currents of the USQ and DSQ at 200 Hz when the EPU gap or phase varies.

Figure 1 shows the optimization process of the EPU66-27 coupling feed-forward table through Bayesian optimization. The optimization process is described as follows:

The program reduces the gap to 16 mm and the phase to 0 mm. In the beginning, 10 sets of initial points are given (the different sets of USQ and DSQ currents and their associated BLM reading). On the basis of these initial measured points, the Bayesian optimization algorithm varies the USQ and DSQ currents to minimize the BLM reading.

#### Verification of Coupling Correction by Closest-Tune Approach

After the creation of the 2D coupling feed-forward table, it is important to verify the performance of the coupling correction. The closest-tune approach² was applied to check whether the minimum gap (tune-split) between the two normal modes was minimized after the correction had been applied. This was achieved by simultaneously scanning the currents of 36 defocusing quadrupoles (referred to as QS1) from -0.49 to -0.88 A relative to their

nominal values, with a step size of 0.01 A. These 36 quadrupoles are located on both sides of the 18 short straight sections. At each step, the turn-by-turn data for 7000 turns from 172 beam position monitors were recorded and converted into betatron tunes using fast Fourier transform. A pulsed pinger magnet was used to excite betatron oscillations to ensure that all 172 BPMs were synchronized with the trigger event initiated by the pinger magnet, allowing the TbT signals to be recorded in sync with the revolution period.

The betatron tunes of the two normal modes were plotted against the QS1 currents relative to their nominal values. The normal mode (eigenmode) tunes can be expressed in terms of uncoupled betatron tunes  $(v_x, v_y)$  and the coupling strength by using the following equation:

$$\nu_{\pm} = \frac{\nu_x + \nu_y - l}{2} \pm \frac{1}{2} \sqrt{\Delta^2 + G_{1,-1,l}^2}$$

, where  $\Delta = \nu_x - \nu_y - l$ , and  $G_{1,-1,l}$  represents the minimum separation between the normal mode tunes. The integer parts of the betatron tunes for the TPS storage ring are 26 and 14 for the horizontal and vertical planes, respectively, resulting in l=12. The minimum gap  $G_{1,-1,l}$  between these two normal modes represents the coupling strength.

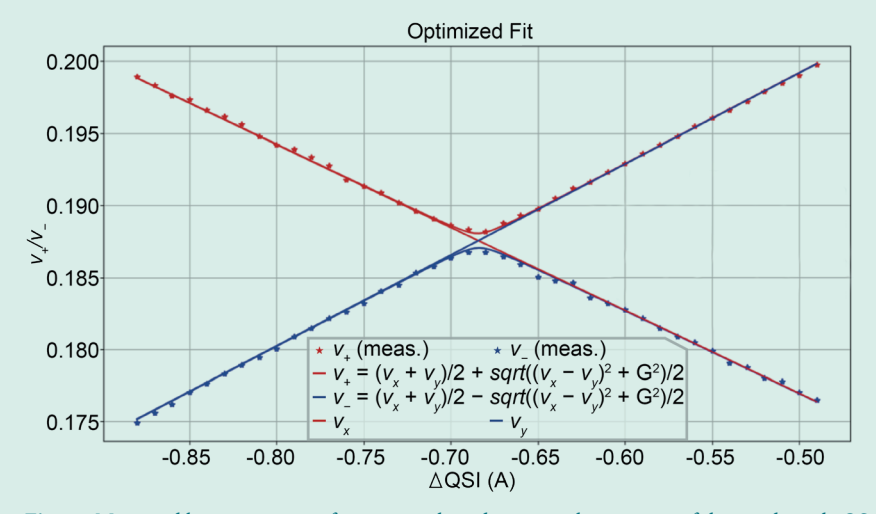


**Fig. 2:** Measured betatron tunes of two normal modes *versus* the currents of the quadrupole QS1 relative to their nominal values for all EPU ID gaps that are open.

**Figure 2** shows the measured betatron tunes of normal modes against the currents of the quadrupole QS1 relative to their nominal values when gaps of all EPU IDs are open. The tune-split  $G_{1,-1,l}$  between the two normal modes is 0.001.

**Figure 3** shows the measured betatron tunes of normal modes against the currents of the quadrupole QS1 relative to their nominal values when the EPU66-27 gap is closed to 18 mm without coupling correction. The tune-split  $G_{1,-1,l}$  between the two normal modes is 0.0046.

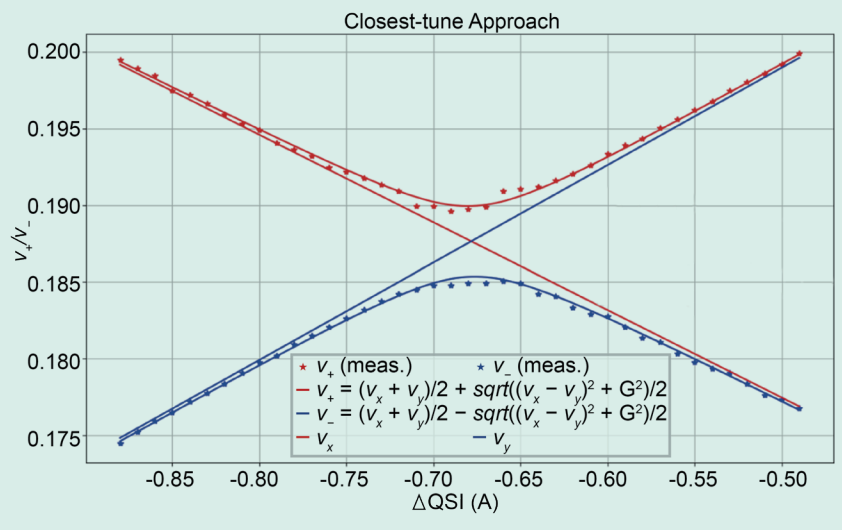


**Fig. 3**: Measured betatron tunes of two normal modes *versus* the currents of the quadrupole QS1 relative to their nominal values when the EPU66-27 gap is closed to 18 mm.

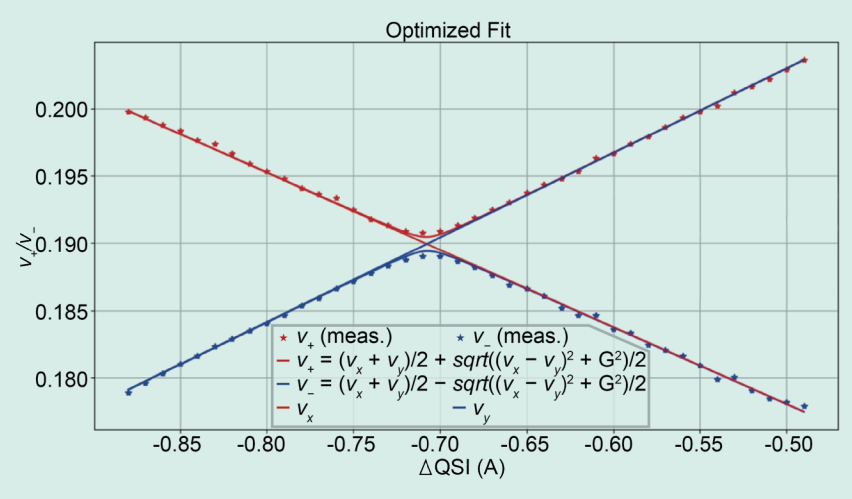


**Fig. 4**: Measured betatron tunes of two normal modes *versus* the currents of the quadrupole QS1 relative to their nominal values when the EPU66-27 gap is closed to 18 mm after coupling correction by USQ and DSQ.

**Figure 4** shows the measured betatron tunes of normal modes against the currents of the quadrupole QS1 relative to their nominal values when the EPU66-27 gap is closed to 18 mm after coupling correction by USQ and DSQ. The tune-split  $G_{1,-1,l}$  between the two normal modes is reduced from 0.0046 to 0.001.

#### Conclusion

Manufacturing imperfections in the EPUs inevitably result in the formation of a residual skew quadrupole component. To mitigate the coupling effects caused by the EPUs and to maintain the vertical beam size, each EPU is equipped with a pair of skew quadrupole magnets. This report demonstrates the feasibility of constructing a 2D coupling feed-forward table based on the gap and phase of EPUs to compensate for the coupling effects using Bayesian optimization. After building this 2D table, the closest-tune approach was employed to verify its performance by checking whether the minimum gap between the two normal modes (tune-split) was minimized after the correction had been applied. (Reported by Mau-Sen Chiu)

- 1. L. Emery, Proc. PAC'**05**, 805 (2005).
- 2. S. Y. Lee, Accelerator Physics, 4<sup>th</sup> edition, Singapore: World Scientific (2021).

## The Path to Sustainability: Energy-Saving Achievements and Future Plans of the NSRRC

The concentration of carbon dioxide in the atmosphere rose from 280 ppm before the Industrial Revolution to 420 ppm. Fortunately, humanity has recognized the climate change problem caused by this issue and has been actively transitioning energy systems. This includes using low-carbon natural-gas power generation as a transitional step and introducing zero-carbon renewable energy sources.

The International Energy Agency compiled data on global power generation for 2020 and 2021 and predicted the energy mix for 2030 and 2050. As shown in **Fig. 1**, while energy demand continues to rise, the share of fossil fuels is expected to drop from 67.5% in 2020 to 25.8% in

2050. Meanwhile, renewable energy is projected to increase from 19.7% to 65.2%, meaning that in 30 years, the roles of renewable and fossil energy will reverse.

**Figure 2** illustrates the power usage and share of major facilities and buildings of the NSRRC in summer. The two accelerators, TLS and TPS, are the largest power consumers, with a combined usage of 4,341 kW. This accounts for 45.3% of the NSRRC total power consumption. The top three subsystems of the accelerators in terms of energy usage are the magnet power supply, radio-frequency (RF) systems, and cryogenic systems. Other major power consumers include the utility systems (3,241 kW, 33.8%), building electricity usage (1,378 kW, 14.4%), and beamlines and laboratories (629 kW, 6.6%).

Using the ISO 14064-1 standard, we record the direct carbon emissions and indirect emissions from purchased electricity of the NSRRC, excluding indirect emissions from employee commuting, business trips, supplier transportation, or service provisions. The annual carbon emissions are about 35,265 tons of CO<sub>2</sub> equivalent, with 95.5% stemming from purchased electricity. The remaining 4.5% comes from kitchen liquid petroleum gas burning, emergency generator operation, official vehicle emissions, refrigerant leaks from air conditioning systems, and experimental processes. Therefore, reducing electricity use is key to decreasing carbon emissions.

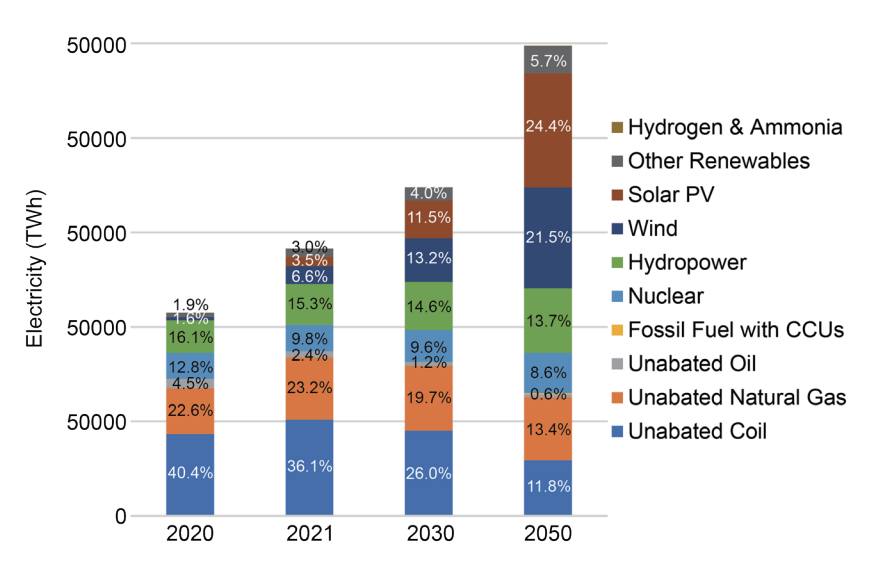
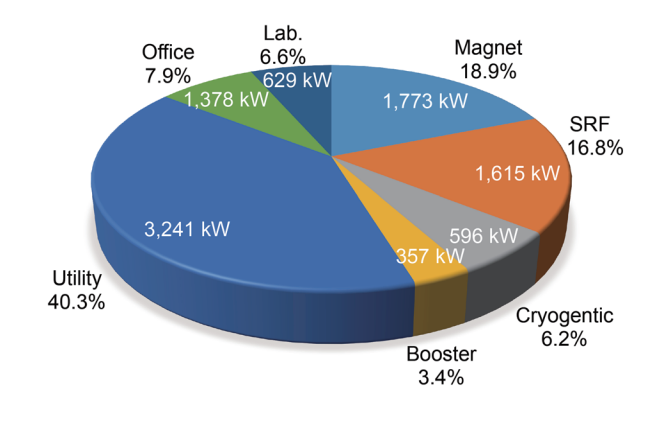


Fig. 1: Global power generation by energy type and percentage.1



**Fig. 2**: Power usage and share by major facilities and buildings in summer 2021 at the NSRRC. [Reproduced from Ref. 2]

From previous energy-flow statistics, it is clear that the accelerators are the most significant power consumers. However, before implementing energy-saving measures, we must consider whether the chosen technologies can affect reliability, safety, investment costs, and economic returns from lower electricity bills. Despite these challenges, recent breakthroughs have been made, such as the energy-efficient operation of booster ring dipole magnets and the implementation of solid-state RF systems in the TPS. Other advancements, such as using permanent magnets, have improved accelerator performance while saving energy, promising further progress.



Fig. 3: Yearly electricity usage statistics for the NSRRC. [Reproduced from Ref. 2]

The second-largest power consumer is the utility system. During the construction of the TPS, energy-saving features like variable-frequency drives for pumps, air-conditioning fans, and air compressors were planned. The NSRRC recently implemented an energy management system, earning ISO 50001 certification. This recognition highlights the energy-saving efforts of the NSRRC and supports the development of new techniques, including:

- A. Optimizing Chiller Operations: Chillers are the core of air conditioning and accelerator cooling systems and the most energy-intensive machines. Connecting the cooling systems with chilled water pipelines across the TLS and TPS allows chillers to be centrally managed for optimal operation and energy efficiency.
- B. Heat Pump Energy Recovery: Waste heat from various equipment and air-conditioning systems can be recovered using heat pumps. This recovered heat can reheat dehumidified cool air to provide the dry, room-temperature air, reducing energy consumption from electric heaters by 70%.
- C. Upgrading to light-emitting diode (LED) in the TPS Experimental Hall: Previously, this area used 384 metal halide lamps, each rated at 400 W. These have been replaced with 153 W LED lights, leveraging improvements in LED lighting technology.

Despite the addition of new equipment and record-high accelerator operation hours, our net electricity usage has decreased yearly thanks to collective efforts. As shown in **Fig. 3**, starting from the TPS's official launch in 2016, and using 2019 as the baseline, the annual electricity consumption of the NSRRC dropped from 72.7 GWh (about 7% of Hsinchu City's household electricity usage) to 66.7 GWh in 2024. This reduction saves at least 6.0 GWh annually, equivalent to TWD 26.5 million in electricity costs. Additionally, the NSRRC has installed solar panels with a total capacity of 1,187 kWp on building

roofs, generating about 1.5 GWh of renewable energy yearly—2.1% of our annual electricity usage. Although the electricity generated is sold to the Taiwan Power Company and cannot be counted toward energy savings or carbon reductions, it provides considerable revenue for the NSRRC.

Saving energy protects the environment and addresses practical concerns such as rising electricity costs and potential carbon fees. From July 2022 to present, electricity rates have increased by 74.8%, and this year's summer rates were extended for an additional month. Energy costs have also been driven up by the war in Ukraine, and carbon fees may be introduced in the future. Under this stress, the NSRRC will continue to implement energy-saving measures such as:

- A. Detecting pipeline leaks
- B. Optimizing operational parameters of mechanical equipment
- C. Recovering heat energy
- D. Replacing outdated equipment
- E. Improving building energy efficiency<sup>3</sup>
- F. Maintaining heat exchangers
- G. Generating renewable energy
- H. Utilizing electrical energy or ice storage systems

By taking these actions, we aim to fulfill our corporate social responsibility and accelerate the transition to green energy. (Reported by Wen-Shuo Chan and Chin-Kang Yang)

- The International Energy Agency, World Energy Outlook 2024, October (2024). https://www.iea.org/reports/world-energy-outlook-2024
- W. S. Chan, "Towards a green accelerator: implementing energy-saving practices at NSRRC" in Proc. IPAC'24, May (2024). https://accelconf.web.cern.ch/ipac2024/pdf/ WEZN1\_talk.pdf
- 3. J. C. Chang, W. S. Chan, Proc. IPAC'23, 209 (2023).

## **Design and Fabrication of a 4 K Helium Phase Separator**

Liquid helium (LHe) is transported from the cryogenic system to superconducting devices through multi-channel transfer lines. However, unavoidable heat loss during transmission causes the LHe to transition into a two-phase flow, which can significantly impact the performance of cryostats in superconducting or other devices not continuously filled with LHe. Helium phase separators were developed at the NSRRC to re-condense the two-phase helium flow from a liquid-helium transfer line and ensure a stable supply of LHe to users.<sup>1,2</sup>

A G-M cryocooler (Sumitomo, model RDK415D) with a cooling capacity of 1.5 W at 4.2 K was integrated into the phase separator to re-condense and liquefy helium while storing it in a 100 L vessel. Practical improvements to reduce the heat load on the helium phase separator were also discussed and implemented.

**Figure 1** depicts the configuration of the helium phase separator.<sup>3,4</sup> The second-stage cold head of the cryocooler, which provides a maximum cooling capacity of 1.5 W at 4.2 K, is connected to an oxygen-free copper condenser mounted at the top of the 100 L LHe vessel. To minimize heat transfer through radiation and convection, the LHe vessel is wrapped in multi-layer insulation (MLI) and housed within a vacuum vessel.

The vessel is supported by four G-10 fiberglass-epoxy rods installed at its base, with the opposite ends secured to the outer vessel to bear the weight of the LHe. Three transfer pipes at the top of the vessel act as inlets and outlets for LHe and as a vent for gaseous helium. Vacuum barriers are placed between the transfer pipes and the outer vessel to mitigate conductive heat loss from room temperature.

A thermal shield made of 30 layers of MLI is connected to the first-stage cold head of the 4 K cryocooler. Positioned between the outer vessel and the LHe vessel, this shield blocks radiative heat loss. Additionally, a thermal bridge made of copper connects the thermal shield to the cryogenic valves, further reducing conductive heat loss. The thermal shield and bridge are constructed of copper, while the outer vessel, LHe vessel, and transfer pipes are made of stainless steel, ensuring durability and effective thermal isolation.

Figure 2 illustrates the piping and instrumentation diagram of the helium phase separator, outlining its operational process. In the first step, the thermal shield was cooled to below 80 K using the first-stage cold head of the cryocooler. Helium gas from the bundle entered the LHe vessel through the pre-cooler, where its temperature was initially reduced. Further cooling occurred *via* heat exchange in the condenser, which was thermally connected to the second-stage cold head of the cryocooler, which brought the helium to its liquefaction temperature.

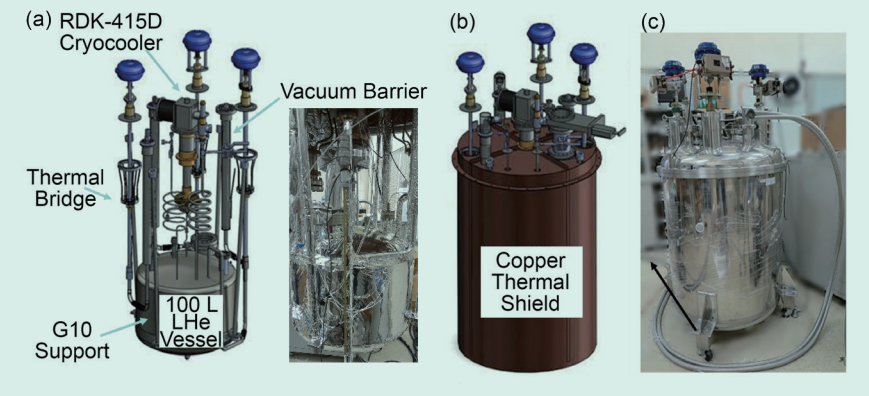


**Fig. 1:** Configuration of the helium phase separator. (a) Components after removal of the thermal shield; (b) outer vessel removed to reveal the thermal shield; (c) prototype of the helium phase separator. [Reproduced from Ref. 3]

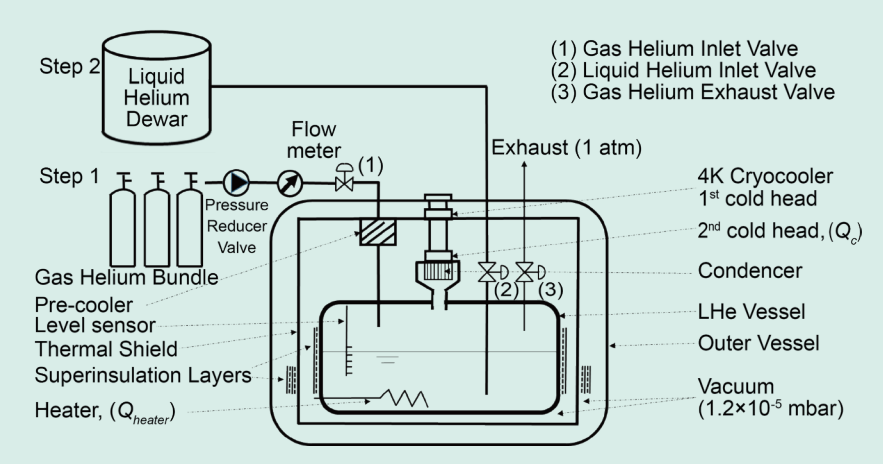


**Fig. 2**: Configuration of the experiment. Step 1: the separator was cooled with the cryocooler. Step 2: the LHe vessel was filled with LHe; the inner heater was then activated to ensure stable operation in this closed system. [Reproduced from Ref. 3]

The pressure in the LHe vessel was maintained at approximately 1.67 bar-a, and key temperatures, including those of the thermal shield, LHe vessel, condenser, and cold head, were monitored. This was done to confirm that the condenser temperature had reached or dropped below the helium liquefaction temperature of 4.8 K at 1.67 bar-a. Achieving this condition ensured helium liquefaction and confirmed that the separator's heat load was within the cryocooler's cooling capacity. This step established the initial cooling and liquefaction process critical for the subsequent liquid-helium operations.

In the second step, LHe was transferred from the dewar to the LHe vessel under the established operating conditions. During the transfer, a portion of the LHe was naturally consumed and vented to the atmosphere through the exhaust valve, which remained open to allow for pressure regulation.

Once the desired operating level of LHe in the LHe vessel was reached, all inlet and exhaust valves were closed, converting the system into a closed configuration. To maintain stable operating conditions, a heater installed in the LHe vessel was activated. The heater's power was precisely adjusted to stabilize both the LHe level and the internal pressure of the vessel. This heating power played a critical role in determining the overall heat load of the system, providing the valuable data for evaluating the thermal performance and efficiency of the helium phase separator.

Helium liquefaction: **Figure 3(a)** illustrates the cooling process of the helium phase separator. The

temperature of the thermal shield dropped below 80 K after approximately 35.9 hours. The condenser temperature reached the liquefaction point of 4.8 K at 1.67 bar-a after approximately 90.8 hours, as indicated by the red point in Fig. 3(a). This marked the initiation of the helium liquefaction process. Figure 3(b) shows the measured helium liquefaction rate, which was approximately 1.4 cm/day, equivalent to approximately 1.8 L/day. The associated thermal parameters were calculated based on data obtained from the Helium Material Handbook and relevant thermodynamic principles, as summarized in Table 1. These data provide insights into the thermal efficiency and performance of the separator during its operational cycle.

LHe storage: Figure 4 illustrates the storage process of

LHe. The LHe level was maintained at 43.4% by activating the internal heater, which was operated at a power of 0.337 W. The internal pressure was stabilized at 1.46 bar-a  $\pm$  0.015 bar throughout the storage period. During this process, the condenser effectively re-condensed the

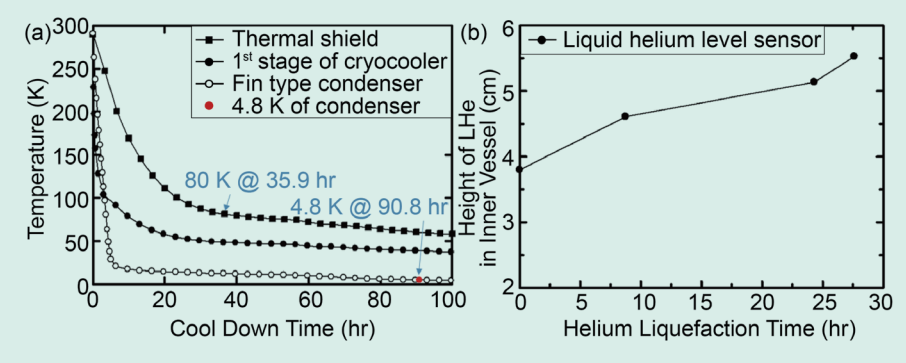


Fig. 3: Experimental results. (a) Cooling-down curve; (b) helium liquefaction rate. [Reproduced from Ref. 3]

Table 1: Thermal parameters.

m	T <sub>e</sub>	h <sub>e</sub>	$T_1$	$\mathbf{h}_1$	$Q_1$	$\mathbf{h}_{2\mathrm{G}}$	$\mathbf{h}_{^{2\mathrm{L}}}$	Qs	$Q_{\rm L}$	$Q_{2nd}$	Q <sub>1st</sub>
(g/s)	(K)	(J/g)	(K)	(J/g)	(W)	(J/g)	(J/g)	(W)	(W)	(W)	(W)
0.0026	295	1532	54	281	3.25	14.06	-1.34	0.69	0.04	0.73	13.8

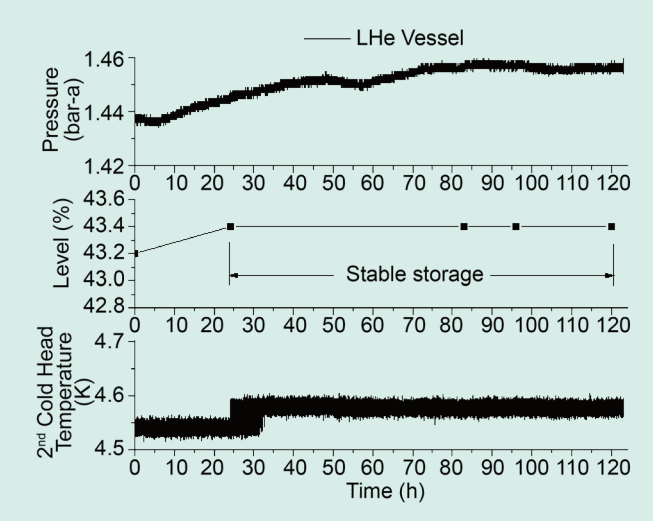


Fig. 4: LHe filling and stable storage. [Reproduced from Ref. 3]

 Table 2:
 Experimental measurements.

Q <sub>heat</sub> (W)	LHe vessel pressure (bar-a)	Level (%)		Second cold-head temperature (K)		Q <sub>load</sub> (W)
0.337	1.46	43.4	35.6	4.59	1.892	1.555

vaporized helium, maintaining a steady state. This stability was sustained for a duration of 96 hours, demonstrating that the heat load of the separator was consistently below the cooling capacity of the cryocooler. This ensured efficient and reliable operation of the helium phase separator during the storage phase.

The experimental data are summarized in **Table 2**. The results indicate that the cooling capacity of the second-stage cold head ( $Q_c$ ) was approximately 1.892 W,<sup>5</sup> as derived from the cryocooler load map shown in **Fig. 5**. The electrical power of the heater ( $Q_{heat}$ ) was measured to be 0.337 W. Using the equation  $Q_{load} = Q_c - Q_{heat}$ , we calculated the heat load of the LHe vessel  $Q_{load}$ , to be 1.555 W. This analysis highlights the effectiveness of the cryocooler in

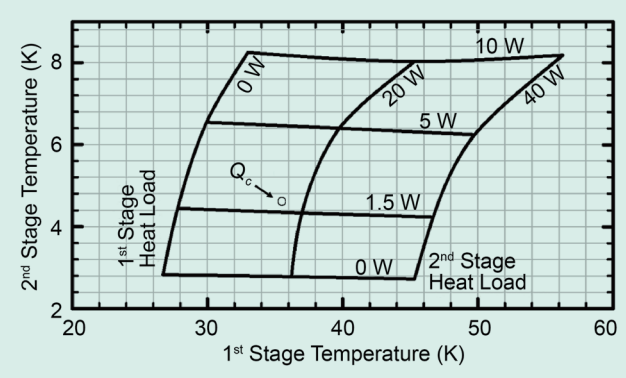


Fig. 5: RDK-415D cold-head load map (60 Hz). [Reproduced from Ref. 5]

maintaining thermal stability while accounting for the heat input from the heater.

During the transmission process, LHe was prone to vaporization due to the heat, leading to the formation of a two-phase fluid within the transmission pipeline. This phenomenon significantly reduced transmission efficiency, hampering the delivery of sufficient LHe and causing instability in user systems.

To address this challenge, the cryogenics group developed a cryogenic freezer re-condensing LHe phase separator. The primary function of this system was to re-condense the two-phase fluid in the pipeline and re-liquefy the separated low-temperature helium gas. The output from the phase separator was high-purity LHe, which effectively minimized the dryness of the LHe in the transmission pipeline, improving the overall stability of the cryogenics system.

The successfully developed re-condensation LHe phase separator could be coupled with a 4 K cryogenic cryocooler to enable zero-boiling operations to condense low-temperature helium. The special design of the radiation isolation baffle further reduced the heat load. In addition to condensing low-temperature helium and storing LHe, the system could convert normal-temperature helium (295 K) into LHe (4 K), functioning as a small-scale liquid-helium production machine.

The system's net cooling capacity was approximately 0.337 W at 4.59 K, with a LHe production rate of approximately 1.8 L per day. The total heat loss was measured at approximately 1.555 W at 4.59 K, showcasing the system's efficient performance. (Reported by Wen-Rong Liao and Chin-Kang Yang)

- 1. H. H. Tsai, F. Z. Hsiao, H. C. Li, M. C. Lin, C. Wang, W. R. Liao, T. F. Lin, W. S. Chiou, S. H. Chang, P. S. D. Chuang, Cryogenics 77, 59 (2016).
- 2. P. S. D. Chuang, W. R. Liao, H. H. Tsai, F. Z. Hsiao, H. C. Li, S. H. Chang, W. S. Chiou, T. F. Lin, Proc. IPAC'16, 1212 (2016).
- 3. W. R. Liao, H. C. Li, P. S. D. Chuang, F. Z. Hsiao, H. H. Tsai, W. S. Chiou, S. H. Chang, T. F. Lin, Cryogenics 96, 108 (2018).
- 4. W. R. Liao, P. S. Chuang, F. Z. Hsiao, H. H. Tsai, H. C. Li, W. S. Chiou, Liquid Generator, R.O.C. Patent No. I614472, (2018). https://tiponet.tipo.gov.tw/S092\_OUT/out
- 5. Sumitomo Heavy Industries, RDK-415D 4K Cryocooler Series, September (2020). https://shicryogenics.com/wp-content/uploads/2020/09/RDK-415D\_Capacity\_Map.pdf

# **Commissioning of Soft X-ray Nanoscopy Beamline at the Taiwan Photon Source**

Commissioning of a soft X-ray nanoscopy beamline at the Taiwan Photon Source 27A (**TPS 27A**) is currently underway. Powered by an elliptically polarized undulator, EPU66, and a newly designed active-mirror plane-grating monochromator (AMPGM), the **TPS 27A** beamline is capable of delivering a photon beam with high energy-resolving power at a constant beam size. Here, we report the commissioning status of beamline **TPS 27A** and its two microscopy endstations: the scanning transmission X-ray microscope (STXM) and photoelectron microscope (photoelectron-related imaging and nano-spectroscopy, PRINS). The STXM endstation is partially opened to users as of the end of 2024, and the PRINS endstation is expected to reach the same status by late 2025.

I. Beamline TPS 27A and 27A1 STXM Endstation

The **TPS 27A** Soft Nanoscopy beamline is designed to deliver a high resolving power and photon flux across a broad photon energy range. To achieve this, a specially developed in-house AMPGM monochromator system with three plane gratings has been implemented. This design supports an energy range from 90 to 3000 eV, with the three gratings covering specific subranges: 90–320 eV, 280–1060 eV, and 1000-3000 eV. Additionally, with the EPU66 undulator system, the photon polarization can be tuned to horizontal, vertical, left-circular, and right-circular states. The beamline is currently in the commissioning stage, which is conducted at the TPS 27A1 STXM endstation. The first X-ray absorption spectroscopy (XAS) of nitrogen gas has been successfully demonstrated, as shown in Fig. 1. The nitrogen K-edge absorption spectroscopy results reveal five distinct vibrational levels in the N1s  $\rightarrow 1\pi_g^*$ transition. Fitting analysis indicates that the full width at half maximum (FWHM) for Gaussian and Lorentzian components are 32 and 110 meV,

respectively. This corresponds to a resolving power of 12,500 at 400 eV, which aligns well with the expected performance. Currently, the commissioning of the 280–1060 eV energy range is nearly complete. Testing for the 90–320 eV range is planned for the first half of 2025, followed by the testing of the 1000–3000 eV range in the second half of the year.

The **TPS 27A1** endstation is designed to perform XAS-related chemical mapping in transmission mode. Its core components include the Zone Plate (ZP) and scanning stages. The STXM endstation is equipped with multiple scanning systems, including stepping motors, piezo walking stages, and piezo actuators with a laser interferometer feedback system. These systems together maintain the relative position between the ZP and the sample, ensuring nanometer-level positioning performance during energy changes and scans, as illustrated in **Fig. 2**. Due to the fundamental properties of ZPs, where the focal length is proportional to the photon energy, the system is carefully designed and fine-tuned to maintain the imaging area with less than 1  $\mu$ m lateral movement across the photon energy range of 280–1060 eV.

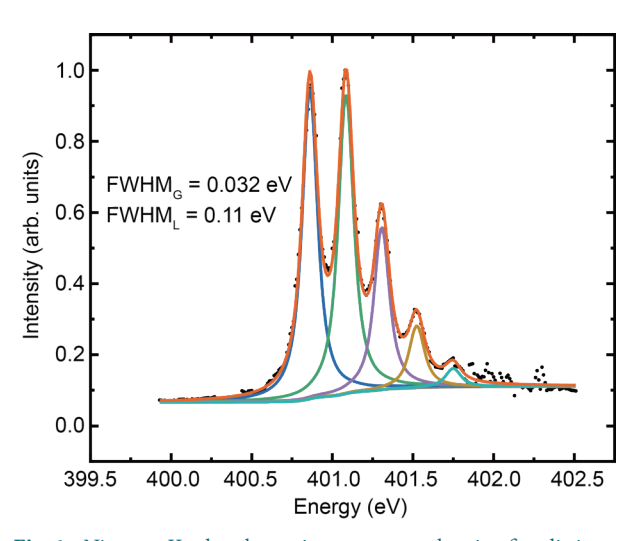


Fig. 1: Nitrogen K-edge absorption spectrum, showing five distinct vibrational levels in the N1s  $\rightarrow$  1 $\pi_g^+$  transition. The fitted curve highlights the high-resolution capability of the beamline.

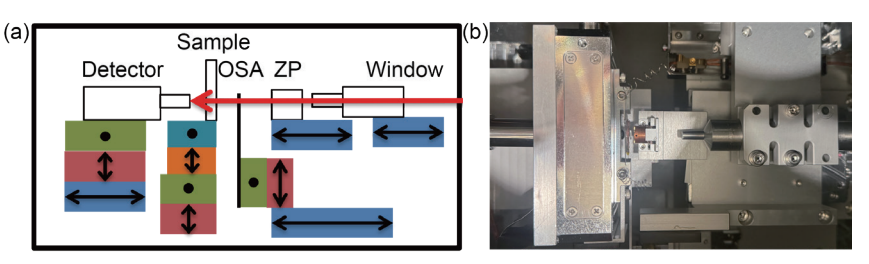


Fig. 2: (a) Schematic representation of the STXM endstation, illustrating the multiple scanning stages, including stepping motors, piezo walking stages, and piezo actuators. (b) Top-view photograph of the STXM endstation, showing the physical layout of the ZP and scanning stages. These components function together to maintain nanometer-level positioning accuracy during energy changes and scans.

Chemical mapping using the spectroscopy capabilities of the STXM endstation is illustrated in Fig. 3. The sample consists of Cu nanoparticles (NPs) doped into g-C<sub>3</sub>N<sub>4</sub>. The STXM elemental mapping, as presented in Fig. 3(a), was conducted at the Cu L-edge and N K-edge. The green region corresponds to the nitrogen signal, while the red region represents the copper signal. These signals were obtained by calculating the difference between the  $\pi^*$  C-N-C peak and the pre-edge for nitrogen, and the Cu main peak and the pre-edge for copper. The corresponding spectra from the Cu L-edge and N K-edge are shown in Figs. 3(b) and 3(c), respectively. The spectrum shown in Fig. 3(b) was acquired from the red regions in the elemental map, which highlight the copper signal. Similarly, the spectrum in Fig. 3(c) was obtained from the green regions, which represent the nitrogen signal. These results demonstrate the powerful capabilities of STXM in combining highresolution microscopy with detailed spectroscopic analysis.

This year, the STXM endstation successfully achieved its first light, marking a significant milestone in its development. Through the current data and commissioning results, we have successfully demonstrated the powerful capabilities of the STXM endstation in delivering highquality nanoscale imaging and chemical mapping. These achievements validate the endstation's readiness to support the advanced research across diverse scientific fields. This cutting-edge STXM endstation is the result of a collaborative effort between the Department of Physics at Tamkang University and the NSRRC, exemplifying the strength of cross-institutional collaboration in driving scientific innovation. To celebrate this milestone, the Opening Ceremony for the TPS 27A1 Nanoscopy Beamline and STXM Endstation was held in late December 2024. Moving forward, commissioning efforts will continue in 2025 to further expand the operational energy range and enable more advanced experimental methodologies.

#### II. TPS 27A2 PRINS Endstation

The **TPS 27A2** endstation aims to perform photoelectronrelated imaging and nano-spectroscopy, and its core is

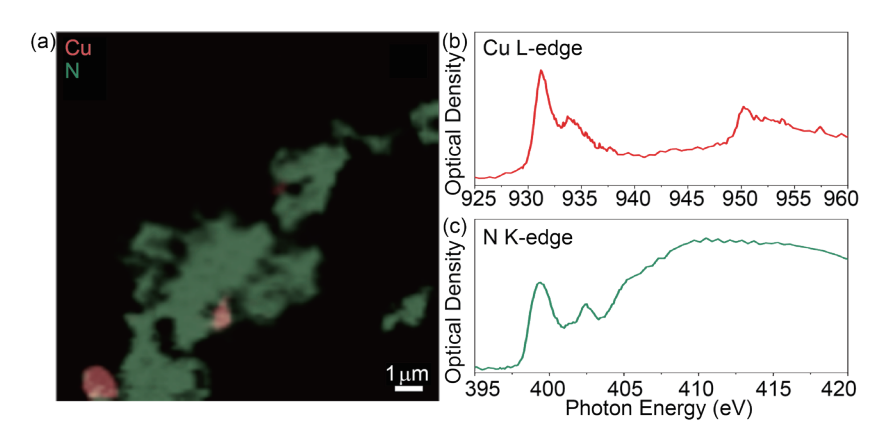
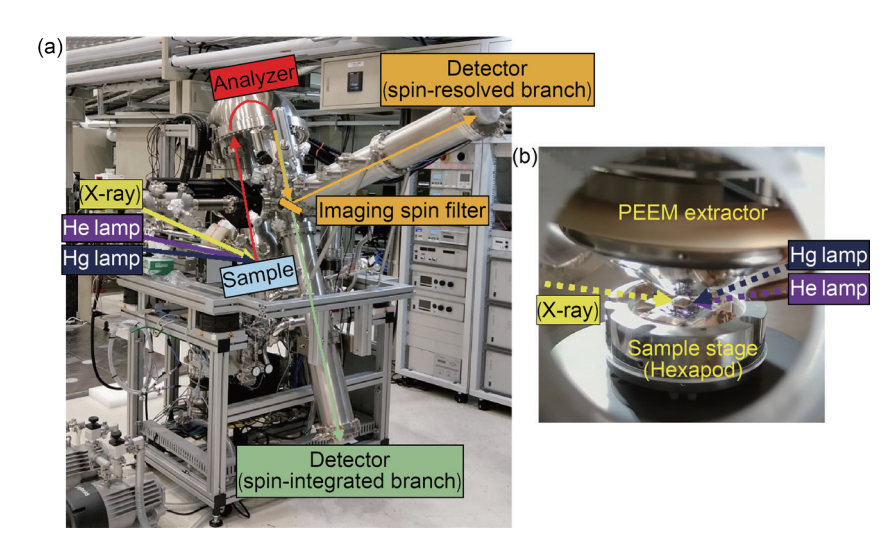


Fig. 3: (a) Elemental mapping of Fe and N for Cu NP/g- $C_3N_4$ . (b,c) Corresponding XAS spectra obtained from the red and green regions, respectively.



**Fig. 4**: (a) Configuration of the photoelectron microscope system at the **TPS 27A2**. The beam paths of photoelectrons are indicated by green arrows for the spin-integrated branch or by orange ones for the spin-resolved branch. (b) Image taken close to the hexapod sample stage, extractor lens, and the capillary of the helium discharge lamp. [Reproduced from Ref. 2]

a photoelectron momentum microscope (MM) system, which is capable of obtaining direct-space imaging, momentum-space imaging, and photoelectron spectroscopy with position sensitivity. The off-line commissioning utilizing both ultraviolet (UV) He discharge lamp and Hg arc lamp has been initiated from mid-2022, and the off-line commissioning results have been reported in early 2024.

The MM system configuration is shown in **Fig. 4**. All light sources, including the soft X-rays and UV lamps, are incident at an angle of 22° relative to the sample surface. The excited photoelectrons are extracted by the extractor lens and projected onto 2D detectors either along the spin-integrated branch or the spin-resolved branch when an imaging spin filter is introduced.

The spatial resolution of direct-space images was tested by analyzing the intensity profile measured on a standard checkerboard-patterned specimen illuminated by the Hg lamp, and the results are shown in **Fig. 5**. The largest field of view (FoV) is approximately 700  $\mu$ m (**Fig. 5(a)**), and the

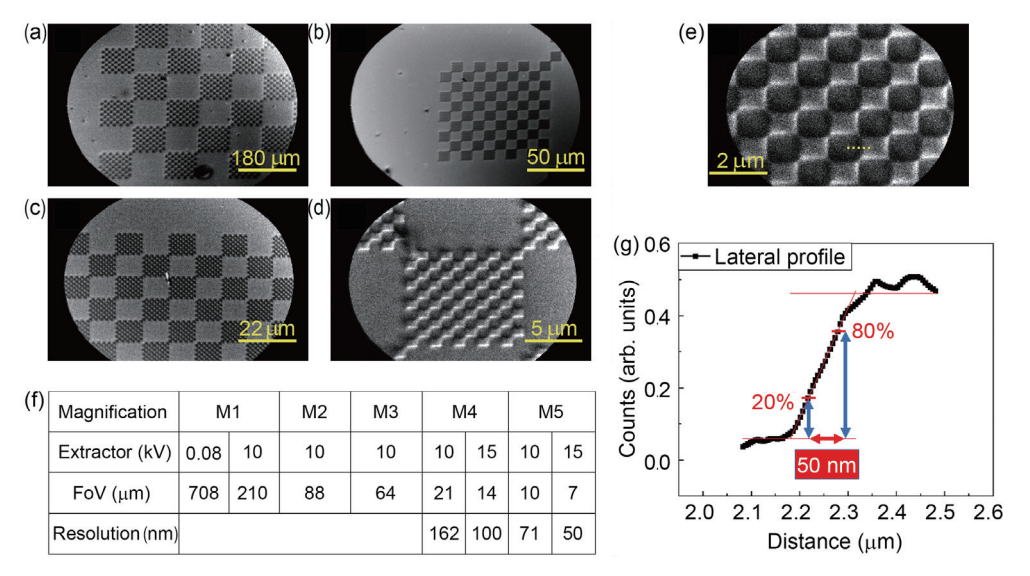


Fig. 5: (a–e) Direct-space photoelectron images of a checkerboard-patterned sample with different FoVs illuminated by the Hg lamp. (f) Table of imaging magnification settings, corresponding FoVs, and resolution. (g) Intensity profile along the edge of the Au patterns marked as a dashed line in (e). [Reproduced from Ref. 2]

smallest FoV is approximately 7  $\mu$ m (**Fig. 5(e)**). Various magnification settings and the corresponding FoVs are listed in the table of **Fig. 5(f)**. The spatial resolution was estimated to be 50 nm by analyzing the intensity profile shown in **Fig. 5(g)** along the edge of the Au patterns, as indicated by a dashed line in **Fig. 5(e)**.

The momentum-space imaging was tested on a Au(111) single-crystal surface by He(I) radiation (21.2 eV), and the results are summarized in **Fig. 6**. A series of momentum-space images exceeding the first Brillouin zone taken at different binding energies are recorded and shown in **Fig. 6(a)**. After stacking all constant-energy contours together to construct a 3D dataset ( $k_x$ ,  $k_y$ ,  $E_B$ ), which is shown in **Fig. 6(b)**, the electronic band structure along any high-symmetry directions can be obtained simultaneously.

In early 2025, more capabilities can be explored using soft X-rays covered by the **TPS 27A** beamline, including the imaging based on XAS, X-ray photoelectron spectroscopy, and X-ray magnetic circular/linear dichroism, which can provide additional element-resolved and magnetization-resolved information. (Reported by Hung-Wei Shiu and Tzu-Hung Chuang)

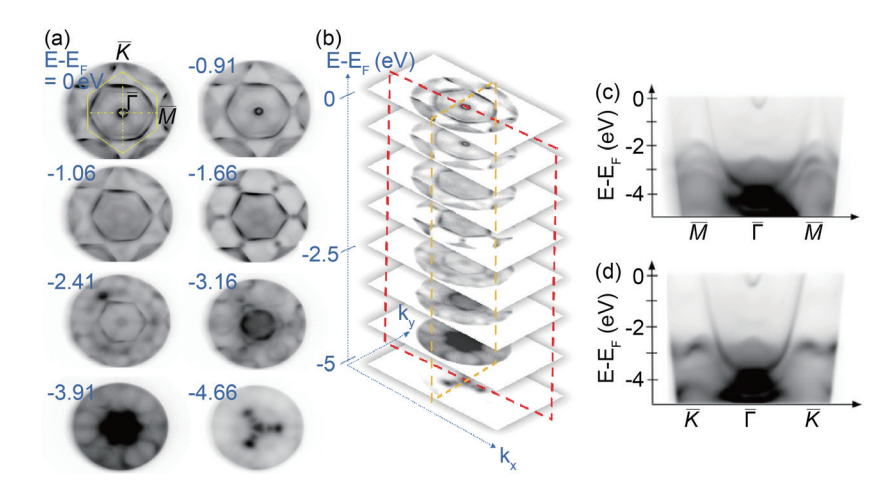


Fig. 6: (a) Momentum-space images recorded at different binding energies obtained from a Au(111) surface at 300 K illuminated by He(I) radiation. (b) Stacking of a series of momentum images with various binding energies, forming a 3D dataset of ( $k_s$ ,  $k_y$ ,  $E_B$ ). (c,d) Slice of the 3D dataset along high-symmetry points of M-Γ-M and K-  $\Gamma$ -K, respectively. [Reproduced from Ref. 2]

- H.-W. Shiu, T.-H. Chuang, C.-M. Cheng, C.-H. Chen, Y.-J. Hsu, D.-H. Wei, J. Electron Spectrosc. Relat. Phenom. 266, 147363 (2023).
- 2. T.-H. Chuang, C.-C. Hsu, W.-S. Chiu, J.-S. Jhuang, I-C. Yeh, R.-S. Chen, S. Gwo, D.-H. Wei, J. Synchrotron Rad. **31**, 195 (2024).

# **Tender X-ray Spectroscopy Beamline at the Taiwan Photon Source**

A tender X-ray beamline, **TPS 32A**, which is part of Phase III of the Taiwan Photon Source (TPS) construction project, has officially opened to users for the 2024-2 cycle. The techniques involve X-ray absorption spectroscopy (XAS) and hard X-ray photoelectron spectroscopy (HAXPES), which are essential tools for investigating material properties at atomic and electronic levels. The **TPS 32A** beamline offers a photon energy range of 1.7–11 keV and delivers a photon flux of 10<sup>12</sup> photons per second at 6 keV. It has two back-to-back double-crystal monochromators (DCMs) that include both Si (111) DCM and InSb (111) DCM configurations. These DCMs enable switching between configurations to meet user requirements. This design ensures enhanced flexibility, particularly for research teams conducting silicon (Si) element measurements. This beamline can measure elemental XAS spectra, including the K-edges of elements from Si to Zn, as well as the L-edges of second-row and third-row transition metals. Additionally, the use of Kirkpatrick–Baez (K–B) focusing mirrors enables the beam to be reduced to a micron-scale spot size, supporting micro-XAS with spatial resolution. These capabilities address the needs of fundamental research and advanced technological innovation, providing cutting-edge experimental

facilities and research resources to academia and industry while opening new scientific frontiers.

The **TPS 32A** beamline integrates HAXPES and XAS techniques, providing users with detailed information on the conduction and valence band electronic structures of materials. As shown in **Fig. 1**, it is divided into four experimental stations: the HAXPES endstation at the focal point, the tender XAS endstation, the hard-XAS endstation, and the micro-XAS endstation.

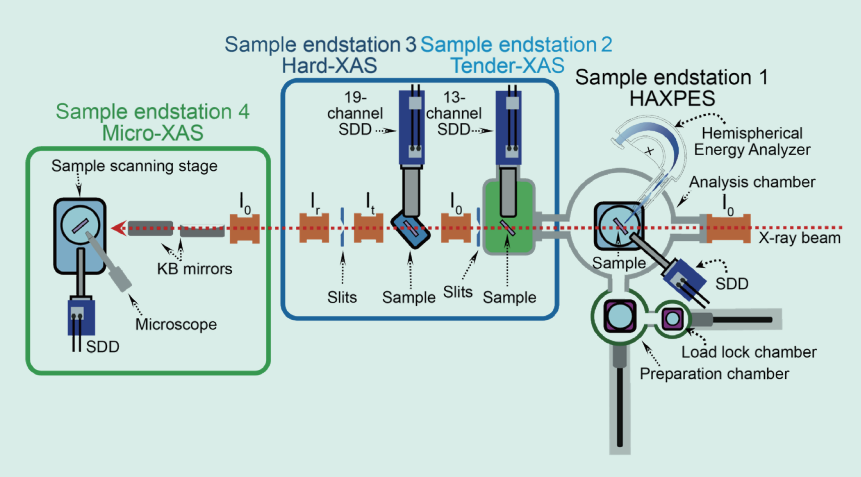


Fig. 1: Layout of the TPS 32A endstations.

The HAXPES endstation, as illustrated in Fig. 2, includes a load-lock

chamber, a preparation chamber, and an analysis chamber. These chambers maintain ultra-high vacuum conditions exceeding 10<sup>-10</sup> Torr. The analysis chamber, which is equipped with a high-performance energy analyzer, can detect photoelectron energies up to 6 keV. By adjusting the incident synchrotron tender X-ray with special photon energies, researchers can access deeper core levels and vary the probing depth of the photoelectron spectra. This capability allows for a comprehensive analysis of the valence band composition and electronic structures of surfaces, heterointerfaces, and bulk regions. In addition, a 7-channel silicon drift detector (7ch-SDD) will be installed in this vacuum chamber to facilitate XAS measurements using the partial fluorescence yield (PFY) mode. This setup enables users to investigate the electronic structure of materials both below (occupied states, HAXPES) and above (unoccupied states, XAS) the Fermi level (E<sub>F</sub>) at the same location on the material.

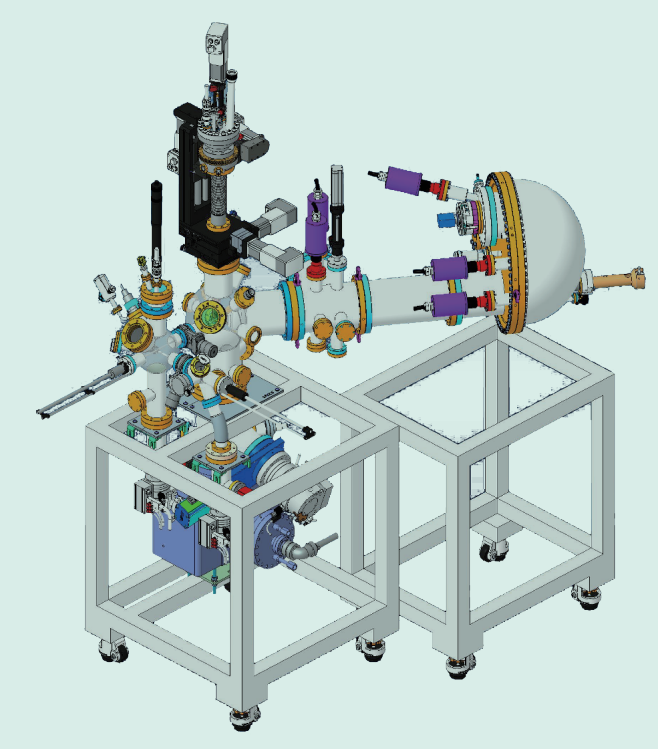


Fig. 2: Schematic drawing of the HAXPES endstation.

Tender XAS endstation is specifically designed for a tender X-ray photon energy range of 1.7–5 keV. The analysis chamber can function in either helium or vacuum mode to minimize photon absorption losses in air at low energies. A load-lock chamber minimizes the time required to stabilize the environment during sample changes. Additionally, a 13-channel silicon drift detector (13ch-SDD) is installed for PFY detection of low-concentration samples, along with simultaneous total electron yield (TEY) measurements. This endstation is designed for measuring the K-edges of silicon, phosphorus, sulfur, and chlorine, along with the L-edges of 4d and 5d transition metals.

The hard-XAS endstation, which covers an energy range of 5–11 keV, is designed for operation under ambient conditions for measuring the L-edges of lanthanides and the K-edges of 3d transition metals. It is equipped with a 19-channel silicon drift detector (19ch-SDD) for PFY mode detection of dilute samples, with sensitivity down to a few ppm. Transmission mode measurements use a grid ion chamber, which offers fast response, a broad linear range, and low background noise. The endstation also supports fly-scan mode, significantly reducing spectral measurement time. For example, Fe K-edge EXAFS scans covering a 1 keV range take approximately 20 seconds in transmission mode and 5 minutes in fluorescence mode.

The endstation is equipped with various *in situ* reaction setups, including electrocatalytic and thermocatalytic reactors and sample cooling systems. Studies of catalytic reactions focus on three main aspects: changes in the catalyst's electronic structure, the formation of intermediates, and the identification of final products. To systematically address these aspects, an advanced electrochemical flow cell integrating XAS, Raman spectroscopy, and gas chromatography–mass spectrometry (GC–MS) has been developed:

**XAS**: High sensitivity to changes in the electronic structure of the catalyst.

**Raman spectroscopy**: Effective for detecting reaction intermediates.

**GC–MS**: Excels in identifying and quantifying final reaction products.

Samples were dispersed on gas diffusion electrodes (GDEs) to facilitate XAS measurements. GDEs feature numerous micro-gas channels to enhance gas diffusion to the catalytic layer. Raman signals are collected through a quartz window, and the final products are analyzed using GC–MS. This setup enables comprehensive studies of catalytic reactions, providing detailed insights into electronic structures, intermediates, and final products to enhance the understanding of reaction mechanisms. This configuration not only enhances the understanding of catalytic processes but also contributes to the development of more efficient catalytic systems.

For thermal catalytic studies, the endstation supports *in situ* measurements at temperatures ranging from room temperature to 1000°C. Samples are placed in capillaries, and reaction gases are introduced through mass flow controllers to allow real-time analysis using XAS, Raman spectroscopy, and GC–MS. This integrated setup, as illustrated in **Fig. 3**, enables a comprehensive understanding of thermal catalytic processes. It allows researchers to investigate the dynamic changes in catalytic materials under the realistic operating conditions. These capabilities are essential for advancing research in fields such as energy conversion, environmental catalysis, and chemical production.

To enhance the efficiency of routine solid-state sample measurements and to minimize errors caused by user unfamiliarity with the operation, the **TPS 32A** has

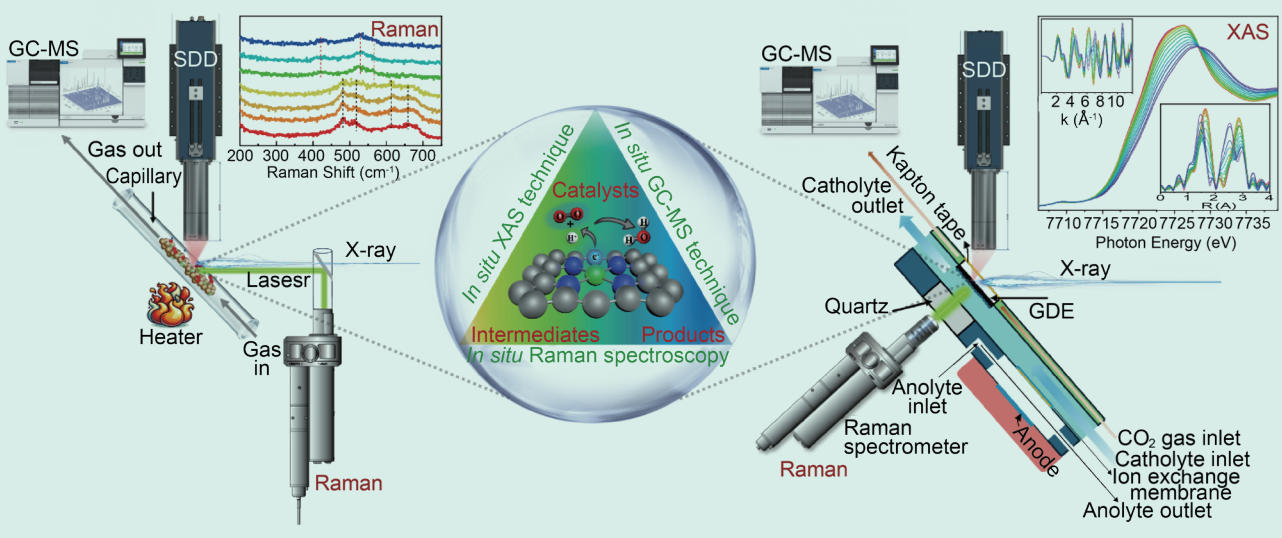


Fig. 3: Schematic drawing of the reaction cell.

developed an automated beamline alignment and sample measurement system. This system improves measurement efficiency and reduces user workload. The automated system comprises the following five subsystems, as shown in **Fig. 4**.

- 1. Automatic filter switching system:

  This system automatically replaces filters for different elements based on measurement requirements, effectively reducing interference from elastic scattering signals. It also helps reduce the occurrence of replacement errors and reduces the frequency of user access to the hutch, thereby improving experimental efficiency.
- Gas switching system: This system
   offers two gas-switching options,
   namely, for high-and low-energy configurations. It
   automatically selects the appropriate gas settings based
   on experimental needs, simplifying the operation
   process.
- 3. Automatic sample changer with robotic arm: This robotic arm system can automatically load and unload samples, accommodating up to 100 samples in a single operation. Without manual intervention, it completes sample changes and automated measurements, significantly reducing the time lost due to the frequent user access to the hutch.
- 4. Sample-position-tracking imaging system: This system accurately tracks the position of the sample, ensuring precise alignment of the X-ray beam with the sample during every measurement. The system automatically moves the beam spot to the sample's center and scans the fluorescence signal intensity to ensure that the beam spot is positioned at the optimal signal strength location.
- 5. Automatic energy calibration system: This system automatically switches calibration foils for different elements, enabling automatic beamline energy calibration without manual adjustments. It simplifies the beamline alignment process and enhances operational efficiency when measuring multiple elements.

These subsystems function in coordination to provide users with an efficient and user-friendly experimental environment, allowing them to focus more on data processing and the analysis of scientific questions.

The micro-XAS endstation, the fourth on the beamline, is positioned at its end. It is equipped with K–B focusing mirrors at its entrance, which focus the X-ray beam to a spot smaller than 10 microns. The endstation is also

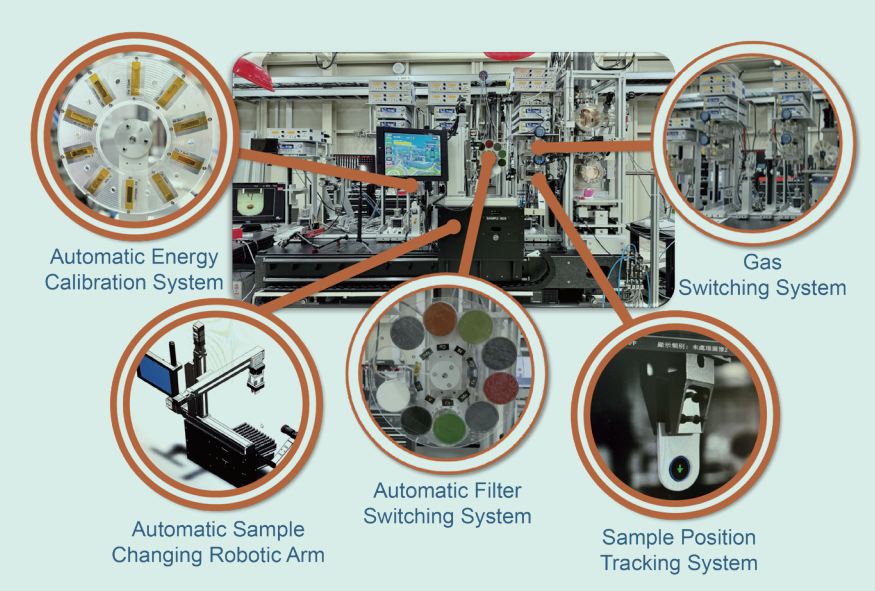


Fig. 4: TPS 32A automation architecture diagram.

equipped with a 7ch-SDD for fluorescence mode detection and includes an optical microscope for sample observation. This setup enables detailed micro-X-ray fluorescence analysis, providing spatially resolved elemental distribution information and facilitating micro-XAS measurements in regions of interest, ultimately offering micron-scale insights into unoccupied electronic states and atomic structures. Micro-XAS offers significant advantages in the fields of energy materials, environmental sciences, and archaeology since it provides high-spatial-resolution analysis of chemical and structural properties.

This report highlights the development of the **TPS 32A** tender X-ray absorption spectroscopy beamline and its endstations. Because of the successful commissioning of the beamline optics and endstations, this beamline has been effectively opened for user access. By incorporating automation and integrating advanced *in situ* analysis techniques, the beamline provides a user-friendly platform for exploring the cutting-edge scientific questions. By the end of 2024, the **TPS 32A** had invited 12 research teams and opened 30% user time for the Proposal Evaluation Committee (PEC) in 2024-2 cycle, resulting in 12 publications. In 2025, **TPS 32A** will open 50% for the PEC cycle and focus on advancing the development and commissioning of the micro-XAS and HAXPES endstations. (Reported by Ying-Rui Lu)

- 1. D.-G. Liu, M.-H. Lee, Y.-R. Lu, J.-F. Lee, C.-L. Chen, J. Synchrotron Rad. **28**, 1202 (2021).
- D.-G Liu, M.-H Lee, Y.-R Lu, C.-C. Liang, C.-F. Chang, J.-L. Tu, J.-F. Lee, C.-L. Chen, J. Vogel, M. Sacchi, S. Iacobucci, J. Phys.: Conf. Ser. 2380, 012041 (2022).